Advances in Science and Technology Research Journal

Advances in Science and Technology Research Journal, 2026, 20(5), 322–334
https://doi.org/10.12913/22998624/215653
ISSN 2299-8624, License CC-BY 4.0

Received: 2025.10.28
Accepted: 2026.03.15
Published: 2026.04.01

Synergistic experimental-numerical study for assessing the aerodynamic performance of a simplified road vehicle

Mohammed Khudhair Abbas[1*], Nazar M. Aldabash[1], Almahdawi Yasseen A.J.[1], Itimad D.J. Azzawi[1], Mudhar A. Al-Obaidi[2]

[1] Department of Mechanical Engineering, College of Engineering, University of Diyala 32001, Iraq
[2] Technical Instructor Training Institute, Middle Technical University, Baghdad 10074, Iraq
* Corresponding author's e-mail: mohammedkhudhair_eng@uodiyala.edu.iq

ABSTRACT

The aerodynamic performance of a simplified prototype vehicle using wind tunnel (WT) experiments and numerical simulations is extensively investigated. The primary aim of this study is to enhance the aerodynamic efficiency of a car model of the 2017 Lamborghini Aventador LP 750-4. Local flow velocity field, pressure distribution, and aerodynamic parameters such as drag and lift coefficients are measured over a wide Reynolds number range in two cases: without a baseline model and with a modified rear wing model. Compared to the baseline model, the modified design achieves a drag reduction of 7.9% and 8.2% numerically and experimentally, respectively. Moreover, the present study has achieved a favourable agreement of 3.39% and 2.98%, respectively, between the numerical drag coefficient reductions for the baseline car model and the modified model. These findings confirm that targeted geometric modifications can significantly reduce drag in ground-vehicle applications and offer guidance for future aerodynamic design.

Keywords: aerodynamic performance, drag reduction, vehicle prototype, wind tunnel testing, numerical analyses.

INTRODUCTION

Environmental and public health requirements have increasingly encouraged the automotive sector to reduce aerodynamic drag as a means of improving vehicle efficiency and operational safety. Over recent decades, transportation engineering has increasingly focused on improving aerodynamic performance. Modifying external body features such as wings, spoilers, and diffusers plays a key role in reducing drag. [1–3]. Although rear wings are widely implemented in racing applications, their influence on passenger-scale vehicles remains insufficiently characterised because most available research focusses on complex, high-end geometries rather than simplified bodies designed for fundamental aerodynamic assessments.

Historically, early vehicle designs with box-type geometries exhibited drag coefficients in the range of 0.7–1.0, whereas modern aerodynamic refinement has reduced these values to approximately 0.2–0.4 [4]. Many studies have shown that geometric optimisation strongly influences wake behaviour, flow separation, and pressure gradients. Bauskar et al. [5] demonstrated that rear-end shaping substantially alters the wake structure and drag for a scaled SUV model, while Wieser et al. [6] showed through DrivAer testing that detailed rear-end configurations directly affect lift and drag performance. The combined use of CFD and wind tunnel testing continues to form the backbone of vehicle aerodynamic development, even small geometric changes can lead to noticeable reductions in aerodynamic resistance [7, 8]. Huluka and Kim [4] found that changing the ducting on a simplified model could cut drag by as much as 15%. Other studies have shown that better body shaping can make EVs and HEVs more energy efficient [9, 10].

Simplified car bodies remain essential tools for assessing how variations in geometry, such as rear slant angles, influence separation and reattachment, which are central to accurate drag and lift predictions [11,12]. The redesign of the Tata Indica using Pro-Engineer V.5 and subsequent CFD testing in ANSYS-Fluent demonstrated how computational methods can deliver significant reductions in drag [13]. Integrating experimental testing with CFD offers a practical platform for detecting aerodynamic issues during early design phases, and several studies have confirmed that vehicles with smaller frontal areas and minimal downforce-producing devices achieve lower drag and higher aerodynamic efficiency [14, 15].

Recent research has expanded toward more comprehensive numerical–experimental frameworks. Al-Saadi et al. [1] employed steady-state Navier–Stokes models and multiple turbulence approaches to suggest improved exterior designs for SUVs. Mohammadi et al. [15] investigated the aerodynamic and structural behaviour of an EV body using an integrated FEM–CFD methodology, demonstrating the capability of advanced simulation tools to generate detailed insights into mechanical and aerodynamic performance. Complementary research by Nowakowski and Kosiuczenko [16] applied FEM to assess the crashworthiness of the TAERO UGV. Furthermore, Qin et al. [7] utilised the DrivAer model in both wind tunnel (WT) and CFD investigations, confirming that hybrid RANS–LES and LES approaches can yield reliable drag and lift predictions.

Despite these advancements, a clear research gap persists. Numerous studies focus on production-grade or high-performance vehicles characterised by intricate geometries or depend solely on computational fluid dynamics (CFD) without stringent experimental validation. Limited work has combined detailed wind-tunnel measurements with numerical simulation for simplified, sports-car-inspired models equipped with aerodynamic devices such as rear wings. In particular, high-resolution experimental pressure and velocity measurements across different Reynolds numbers remain scarce. Such simplified models are indispensable for understanding flow mechanisms and for benchmarking computational approaches.

This work introduces a simplified vehicle prototype based on the proportions of the 2017 Lamborghini Aventador LP 750-4. The design preserves key aerodynamic characteristics while avoiding excessive complexity, making it suitable for controlled wind-tunnel testing and CFD validation. The prototype, fabricated through 3D printing, was evaluated experimentally in the subsonic WT at the University of Diyala–College of Engineering (UOD-COE). Local velocity and static pressure distributions were measured using a digital manometer (AHJ-501) and a hotwire anemometer (Testo 425) across varying Reynolds numbers, and complementary CFD simulations were performed to analyse flow behaviour and validate the experimental observations.

The simplified model selected for this study provides a scientifically robust basis for examining how targeted geometric modifications—particularly the addition of a rear wing—affect drag, lift, pressure distributions, and overall aerodynamic behaviour. The integrated experimental–numerical approach aims to narrow the research gap identified in the literature, offering value for future aerodynamic optimisation of passenger vehicles and high-efficiency designs. The rest of this paper is organised as follows: Section 3 describes the experimental methodology and wind-tunnel configuration; Section 4 presents the validation of numerical and experimental data; Section 5 reports and analyses the aerodynamic results; and Section 6 outlines the main conclusions and future research directions.

SETTING UP THE WIND TUNNEL AND CONDUCTING THE EXPERIMENTS

The aerodynamic experiments were performed in the open-loop WT located in the Mechanical Engineering Laboratory at UOD-COE (Figure 1). The tunnel consists of a bell mouth with an air straightener, a settling chamber, a contraction cone, a transparent acrylic test section, and a diffuser. Before operating the system, the apparatus was accurately levelled to ensure horizontal alignment. After activating the three-phase power supply, airflow was generated using a variable-speed motor producing velocities from 0 to 30 m/s, corresponding to a maximum Reynolds number of approximately 7×10^5. The tunnel structure is made of fiber-reinforced plastic, and the smooth test section walls minimise surface roughness effects relative to the model scale. The test section dimensions are $0.32 \times 0.32 \times 0.53$ m. The blockage ratio in the test section was below 5%, which is generally considered acceptable for subsonic automotive testing.

Figure 1. Wind tunnel of UOD-COE

A 25 × 0.5 cm slot was incorporated into the upper wall of the test section to accommodate a 2 mm copper tube and the hot-wire probe. Through this access, velocity and pressure were measured at 14 stations: point 1 upstream, twelve locations above the upper surface, and point 14 downstream (Figure 2a–b). The model was placed directly on the test-section floor and held in position from above, consistent with the tunnel's structural design. Air velocity was recorded using a Testo 425 hot-wire anemometer (accuracy ±0.03 m/s), and static pressure was measured using an AHJ-501 digital manometer (accuracy ±0.3% FSO, resolution 10 Pa). The flow entering the test section exhibited a uniform velocity profile with deviations below ±1.5%, and turbulence-intensity levels were 6.7% and 5.6% as measured by the hot wire and manometer, respectively. Measurement corrections were applied to account for freestream-velocity and static-pressure uncertainties. Repeated, time-averaged readings were taken under controlled temperature conditions to ensure reliable measurements. The hot-wire probe operated slightly outside its calibration range, but the resulting uncertainty remained acceptable (0–0.15 m/s), the resulting uncertainty remained below 2% at higher speeds. Table 1 lists the complete instrumentation specifications.

Due to the tunnel configuration, accessing the region beneath the model was not possible without

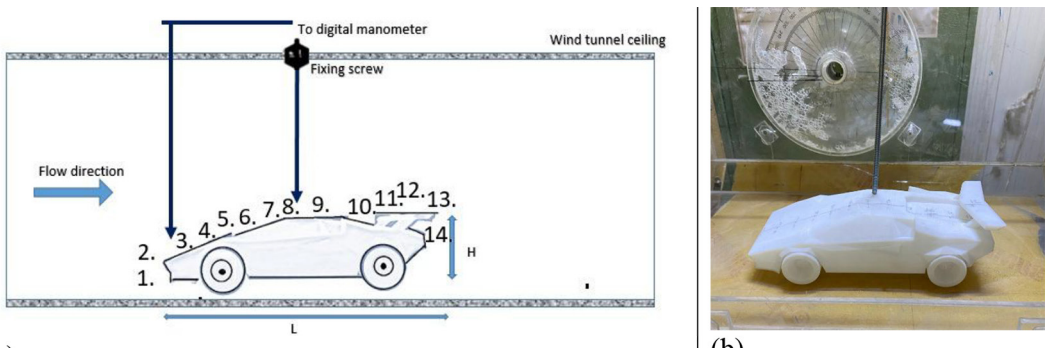

(a) (b)

Figure 2. (a) Schematic (b) experimental model for the car model within the wind tunnel section

Table 1. Specification of wind tunnels (WT) in the UOD-COE

Type	Open wind tunnel (WT)
Duct material	Fibre-reinforced plastic
Speed variation	10% to 100% (controlled via a frequency drive controller)
Test section material	Acrylic sheet (10 mm thickness)
Blower Fan	8 blades
Motor	AC motor, 3480 RPM, 12 HP
Air Length	4.58 m
Turbulence intensity	0.05
hot wire (Testo 425)	Measuring ranges: 0.1 to 30 m/s, - 20 to 70 °C. Resolutions: - 0.01 m/s, 0.1 °C. Measuring ranges: 0.1 to 30 m/s, - 20 to 70 °C Accuracies: - ± (0.03 m/s + 4.0 % of mv) (0.01 to +20 m/s), ± (0.5 m/s + 5.0 % of mv) (20.01 to +30 m/s), 0 to 60 °C; ± (0.5 °C).
Digital manometer (AHJ-501)	Accuracy: ± 0.3% FSO (25 degree), readability± 0.2% (Max+/-0.5%FSO), Pressure Range: ±2.999 psi

altering the mounting or damaging the tunnel structure; therefore, the pressure distribution was evaluated only on the upper surface. While full pressure integration over both surfaces is ideal, the available measurements provide sufficient resolution to characterise the flow above the model and assess the comparative aerodynamic trends investigated in this study. The streamlined vehicle prototype was inspired by the proportions of the 2017 Lamborghini Aventador LP 750-4. The 5% scaled model was intentionally simplified by removing vents, recessed grooves, electronic elements, and underbody details while preserving the essential aerodynamic form. This reduction in complexity improves printability, ensures a clean flow field, and isolates the aerodynamic contribution of the rear wing.

After completing the CAD model, the vehicle was fabricated in plastic using a Creality K1 Max 3D printer at a specialised facility in Baghdad. The same CAD geometry was later employed in the numerical simulations. Table 2 presents the dimensions of the car model, rear wing, wind tunnel test section, and frontal area, confirming that the blockage ratio remained below 7.5%. The resulting prototype features a rigid body with streamlined contours and rotating wheels, suitable for stable mounting and accurate aerodynamic testing. Figure 3 shows both the numerical and experimental models used in this study. A 5% scale was selected to ensure geometric fidelity while maintaining a blockage level below the recommended limit for closed-test-section wind tunnels and allowing the model to be fabricated with sufficient surface precision

Experimental methodology calculation

To calculate lift and drag coefficients and lift and drag forces, the upstream (point 1) and downstream (point 14) velocities, which are shown at

Table 2. The characteristics of both the experimental and numerical car models

All dimensions in mm		Experimental	Numerical
Dimensions of car model	Length, L_m	229	223
	Width without mirrors, W_m	102	99
	Height, H_m	46.75	47
Wind tunnel section and total dimensions of the computational domain	Long, L	530	750
	Width, W	230	300
	Height, H	230	350
Rear wing dimensions	Height, H_R	30	30
	Width, W_R	5	5
	Long, L_R	68	68
Frontal area, Af	mm^2	4768.5	4653
Blockage ratio, B	%	4.66	4.43

the point before and behind the car model, were recorded using a hot-wire instrument. Additionally, the static pressure and pressure coefficient in these areas were measured using a digital manometer. Twelve locations above the vehicle's surface centerline were also used to record velocity and static pressure. Equation 1 is used to compute an actual drag force [17–19].

$$F_{d_{act}} = 0.5\,\rho\,A_f\left(V^2_{upstream} - V^2_{downstream}\right) \quad (1)$$

where: V_{up} represents the upstream velocity, $V_{downstream}$ denotes the downstream velocity, A_f is the frontal area of the scale model, and r indicates the density of air.

The theoretical drag force is calculated using upstream velocity only, as depicted in Equation 2 [17].

$$F_{d_{the}} = 0.5\,\rho\,A_f\left(V^2_{upstream}\right) \quad (2)$$

The ratio of actual drag force to the theoretical drag force is represented by the drag coefficient (*CD*) [17].

$$C_D = \frac{F_{d_{act}}}{F_{d_{the}}} \quad (3)$$

The blockage ratio measures the degree to which the vehicle obstructs airflow in the wind tunnel. One of the most crucial elements influencing the precision of aerodynamic measurements is the blockage ratio, which is stated in Equation 4, which is recommended to be less than 7.5% in wind tunnel testing [17].

$$B = \frac{A_f}{A_w} \quad (4)$$

where: A_w is the area of the wind tunnel section.

The pressure coefficient of the flow on car surfaces is defined in Equation 5 [17].

$$Cp_{,i} = \frac{P_i - P_\infty}{q} \quad (5)$$

where: P_i represents the local surface pressure, and P_∞ static denotes the far-field static pressure.

Reynolds number is defined in Equation 6 [13].

$$Re = \frac{\rho\,V\,D_h}{\mu} \quad (6)$$

where: D_h is the hydraulic diameter of the square test section of the wind tunnel, and μ is the dynamic viscosity of the air.

The dynamic pressure (q) can be calculated using Equation 7 [13,14].

$$q = 0.5\,\rho V^2_{upstream} \quad (7)$$

The lift force can be estimated using this formula.

$$L = \sum_{i=1}^{N}\left(P_i - P_\infty\right) A_i \quad (8)$$

The lift coefficients can be derived from integrated surface pressure distributions (Cp values), then the lift coefficient is determined using Equation 9 [17].

$$C_L = \frac{L}{qN} \quad (9)$$

where: N is the number of nodes, and L is the lift force.

Traditional aerodynamic experiments use 6-component force balances to measure lift and drag. However, the UOD wind tunnel does not include a force balance suitable for models of this size and mounting type. Because of this, a pressure-based approach was utilised. This method tallied up the surface pressures that were spread out to provide an approximation of the aerodynamic stresses. This method is frequently employed in small-scale experimental aerodynamics when force balances are unavailable or incompatible with the model's support structure.

A complete uncertainty analysis was done to find out what would have caused the errors in the pressure acquisition system, tubing response, manometer resolution, and alignment tolerances. The overall uncertainty in the combined drag and lift forces was determined. We used the uncertainty equations for random and systematic factors to determine how accurate the hotwire and digital manometers were and how much inaccuracy there was in the measurements. In this case, data were taken from the manufacturer's specifications for pressure taps and hot-wire velocity instruments. For example, Table 1 shows the Testo 425 hot wire accuracy and the AHJ-501 manometer accuracy of ±0.3% FSO. hot-wire (speed V): The equation ΔV = 0.03 + 0.04 V provides the tolerance at speeds V of 20 m/s or less. Assuming a rectangular distribution, this tolerance can be converted into a standard uncertainty in velocity reading as stated by [17].

$$u_V = \frac{\Delta V}{\sqrt{3}} \quad (10)$$

Referring to the pressure digital manometer, uncertainty reading can be deduced in the following formula.

$$u_P = \frac{\Delta P}{\sqrt{3}} \tag{11}$$

Uncertainty (u) reading in pressure distribution above the surface of the car model can be estimated using Equation 12 while considering the analytical partial derivative linear propagation for aerodynamics (Equation 5 and 7),

$$u_{Cp,i} = \sqrt{(\frac{1}{q}u_{p,i})^2 + (\frac{-1}{q}u_{p,i})^2 + (\frac{\partial C_{P,i}}{\partial V_{upstream}} u_{Vupstream})^2} \tag{12}$$

The uncertainty in lift coefficient contribution is as follows:

$$CL_i = \frac{C_{P,i}A_i}{A_f} \tag{13}$$

$$u_{CL,i} = \frac{A_i}{A_f} u_{Cp,i} \tag{14}$$

The total lift coefficient $CL = \sum_{i=1}^{N} CL_i$ and the uncertainty in lift coefficient are:

$$u_{CL} = \sqrt{\sum_{i=1}^{N} u^2 CL_i} \tag{15}$$

And the uncertainty in drag coefficient can be calculated using Maskell [21]and Mercker [22] approach as:

$$CD_{corrected} = \frac{CD_{measured}}{1+kB} \tag{16}$$

where: k is the shape parameter of bluff vehicle = 1.85–2. An interested reader is referred to Chen Fu. et al. [23] for further details.

Geometric deviations and manufacturing tolerances

Geometric deviations show the discrepancies between the CAD model and the actual 3D-printed prototype that are caused by restrictions in the manufacturing process. Manufacturing tolerances set the limits on what is acceptable and make sure everything works right. We used a Vernier calliper (±0.02 mm) to measure the testing model, and Table 3 compares the key external dimensions of the CAD model, 3D-printed wind-tunnel model, and the simplified CFD geometry used in the simulation. The surface roughness of the 3D-printed model was Ra ≈ 11–14 µm, typical for FDM printing. Using published correlations [17,18], the maximum geometric deviation (1.18%) leads to an estimated uncertainty in the drag coefficient of ≈ 0.6–1.4%. A blockage ratio below 5% is considered negligible and does not qualitatively affect aerodynamic trends. In addition, the numerical model is purposefully smoother and somewhat shorter in width and length, which is in line with CFD meshing criteria and what is done in the literature [13]. The differences are within the acceptable limits for CFD–WT comparisons.

NUMERICAL ANALYSIS

The second part of this study is the numerical analysis of the car model. The geometry includes a rectangular part that holds the car model. Figure 3 (a) shows the computational domain. The area behind the car should be long enough to allow for flow separation without interfering with air flow in the output portion. It should also be lengthy enough to demonstrate the wake zone. The boundary condition (BC) accurately reflects the actual condition. In ANSYS Workbench, the Fluent v.15 solver shows the BCs like this: The flow velocity at the inlet was utilised to ascertain the flow velocity. The input velocities in this investigation are perpendicular to the boundary. The pressure outlet was adjusted to the outlet boundary, the pressure gauge was set to zero, and the symmetric boundary conditions of the top wall and side walls were modelled. The shear stress transport k − ω (SST) turbulence model was used with a turbulence intensity of 0.5% and convergence criteria (all residuals ≤ 1 × 10^{-6}; 1000 iterations), as shown in Figure 3(b).

To determine the most suitable mesh resolution, a detailed mesh sensitivity analysis was performed. There were twelve simulations run for the automobile study case, with each case using a different level of mesh refinement. The process began with a coarse mesh in the initial simulation, followed by gradually finer meshes in the subsequent runs until the differences became minimal and fell within an acceptable error range,

Table 3. Geometric deviations between CAD, CFD and Printed model

Parameter	CAD (mm)	Printed model (mm)	Deviation (mm)	% Error	CFD model (mm)	Max % difference
Length	229	228.4	-0.6	0.26%	223	2.6%
Width	102	101.3	-0.7	0.69%	99	3%
Height	46.75	46.2	-0.4	1.18%	47	1.7%

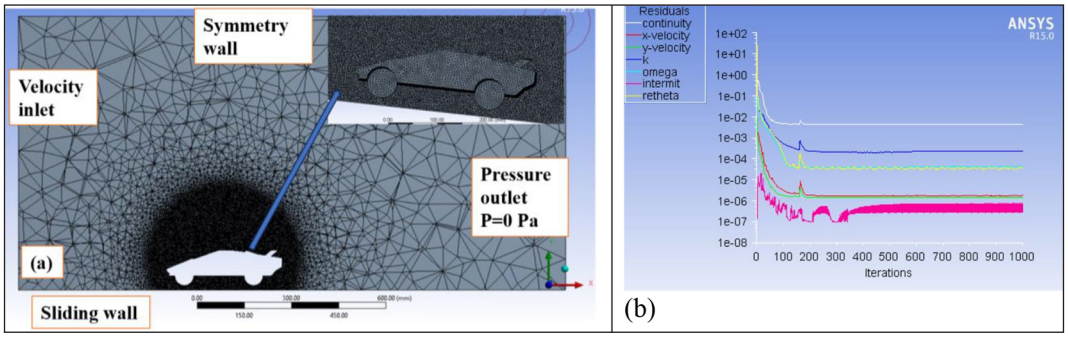

Figure 3. (a) Meshing of the model with the boundary conditions (b) The residual at the inlet velocity is 27.3 m/s

indicating mesh independence [10, 14]. Structured meshes are usually easier to use and provide you more access to data. Unstructured meshes, on the other hand, are more flexible and work well in tough areas. High-quality hybrid meshes take advantage of the best parts of both methods. The most recent calculations employed the tetrahedron mesh to figure out how the flow field surrounding the automobiles worked, and the minimum mesh skewness is 1.81×10^{-5}. To complete this work, the y+ value had to stay (min = 0.089, mean ≈ 15.47, max = 58.67). This y+ range is consistent with wall-function requirements for the SST k–ω model.

A refined mesh is generated in proximity to the vehicle surface to provide a precise estimation of the velocity profile near the wall, maintaining the y+ value within the range of 20 to 200, which is considered optimal [7, 20]. The number grid is in the symmetry plane, which is close to the automobile body. It had well over 3,000,000 cells, and the grid was refined close to the surface of the body and in the wake region. More grid refining showed that the results presented were not wholly new. The findings showed that finer meshes can still influence the accuracy of the results, highlighting the importance of balancing computational time with simulation precision. The outcomes of the mesh independence test are illustrated in Figure 4, and the uncertainty value found from the standard error from the nonlinear least squares fit is ± 0.0071 for a 95% confidence level.

LIMITATIONS

The findings of this study must be interpreted in light of several methodological and geometric limitations.

Simplified geometry

The model excludes fine exterior details (vents, underbody structures, curvature transitions), which are known to alter wake dynamics. While this simplification enables controlled aerodynamic comparison, the absolute CD and CL values may differ from full-scale vehicles by 5–12%, consistent with Hucho [17] and Delassaux et al. [13].

Blockage-ratio

Impact the blockage ratio of 4.66% (experimental) is below the recommended 7.5%, but still introduces measurable bias. Using Maskell's

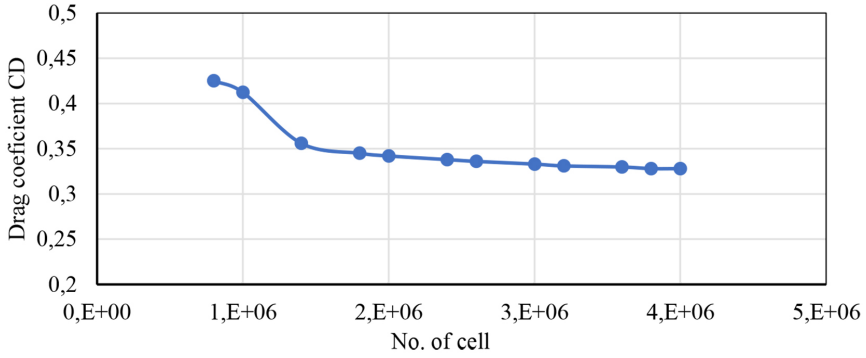

Figure 4. Variation of drag coefficient against the number of cells throughout the grid dependency test

correction, the measured drag is overestimated by ≈ 8%. Corrected values are provided in Section 5.

Upper-surface-only pressure integration

Due to constraints of the wind-tunnel mounting system in UOD-COE pressure data were collected only on the upper surface. SAE and Hucho data indicate that excluding the underbody typically underestimates total drag by 8–12%. Thus, the present drag values should be interpreted as upper-surface contributions only, not full-body drag.

Measurement uncertainties

Uncertainties arise from:
1. Hot-wire accuracy limits (~2% at high speed),
2. Manometer resolution (±0.3% FSO),
3. Probe-alignment tolerances (±0.5 mm),
4. 3D-printing dimensional deviations (~1.2%).

Combined influence leads to estimated uncertainties of:
- $u(C_D) \approx \pm 0.024$(exp.)
- $u(C_L) \approx \pm 0.021$(exp.)
- geometry-related CD bias: 0.6–1.4%.

Applicability to full-scale vehicles

Scale effects, Reynolds-number limitations, and geometric simplifications prevent direct translation of absolute CD values to full-size cars. However, relative trends, such as the effect of the rear wing on pressure distribution and wake stabilization, remain reliable and physically meaningful. The experiments were conducted with a stationary ground plane, which does not fully reproduce the moving-ground condition of real vehicles. The absence of ground motion typically leads to a slightly thicker boundary layer and earlier separation near the underbody, which may influence the absolute drag and lift values; however, relative trends between the baseline and winged configurations remain physically meaningful.

RESULTS AND DISCUSSION

The investigation started by examining the flow around a fixed, basic automobile design, where the outcomes served as the benchmarks. A rear wing was added to the car model numerically and experimentally. The study's objective was to examine how the inclusion of more movable aerodynamic components can affect the body's aerodynamic properties while comparing their results against the simulation ones. The results of the examination of the flow area close to the vehicle include the drag and lift coefficients, the distribution of pressure coefficient Cp values along the automobile's surface at various Reynolds numbers, and the local velocity distribution along the vehicle's surface. The pressure coefficient Cp and local velocity distributions vary along the surface of a basic car model for different Reynolds numbers.

Figure 5 presents a comparison of the numerically and experimentally determined drag coefficient of the 2017 Lamborghini Aventador LP 750-4 car model with and without a rear wing across different Reynolds numbers, revealing how aerodynamic performance shifts with flow conditions. At lower Reynolds numbers, the presence of the rear wing leads to an approximately 5% and 8% increase in drag experimentally and numerically, respectively, due to greater wake turbulence and flow separation in viscous-dominated regimes.

Additionally, to assess the uncertainty in the experimental and numerical measurements at the specified confidence level, the absolute mean difference between these measurements was found to be 0.0104, with a standard deviation of 0.0033 for cases involving a rear wing; all experimental results fall within ± 0.08 of the numerical predictions at an uncertainty level of (k=2). The experimental and numerical drag coefficients (CD) with and without the rear wing exhibited the same trend and agree within measurement error. The numerical and experimental findings appeared to be compatible at the 95% confidence level. The Guide to the Expression of Uncertainty in Measurement ascertained that uncertainty assessment should be done by analytically propagating the tolerances of the instruments (hot-wire and digital manometer).

The Maskell method is used to resolve blockage effects so that the measured drag takes into account how the test-section confinement affects it. When the model is in the test-section area, the flow around it speeds up, which makes the drag coefficient too high. By using the Maskell's adjustment corrects and when the shape parameter k is set to 1.9, the blockage correction approach yields a drag coefficient of approximately 0.919, indicating that the uncorrected drag coefficient overestimates by about 8.1 %, as shown in Table 4. Integration just of the upper surface is recognised to underestimate overall drag, as the

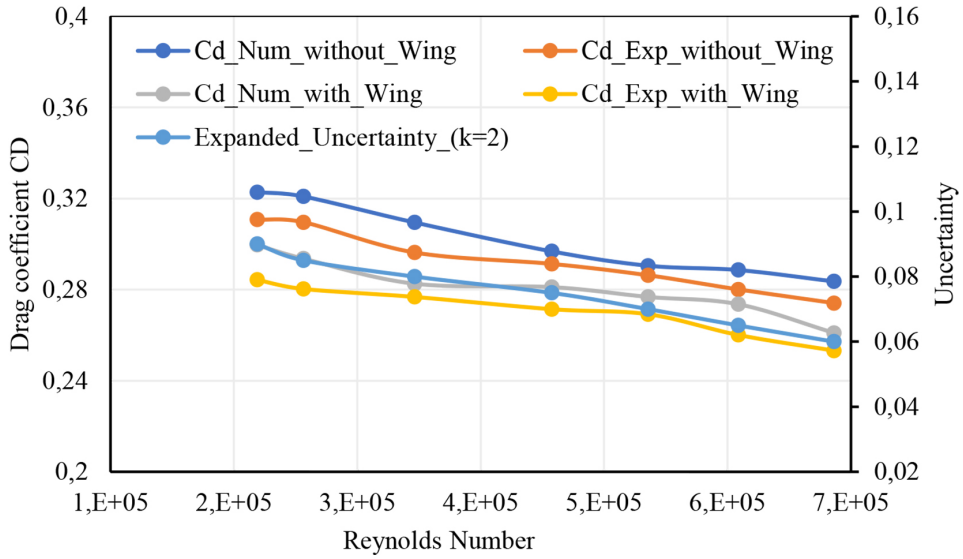

Figure 5. Comparison between experimental and numerical uncorrected drag coefficient CD with and without using a rear wing at different Reynolds numbers

Table 4. CD measured and CD corrected

Case	Cd (measured)	Cd (corrected)	Percentage overestimate
Baseline	0.2741	0.2519	8%
Modified	0.2532	0.2326	8.1%

underbody strongly contributes through pressure drag and shear forces. Hucho [17] and SAE studies on simplified vehicle bodywork indicate that excluding lower-surface pressures often leads to an 8–12% underestimation of total CD. The current configuration indicates an estimated bias of approximately 10%, suggesting that the actual full-body drag is likely greater by this margin.

To contextualise the aerodynamic performance of the tested configurations, the obtained drag and lift coefficients are compared with the well-established ranges reported by Hucho [17] for typical passenger-car geometries. Such a comparison provides an external benchmark to assess whether the present baseline model and the wing-equipped configuration fall within the expected aerodynamic behaviour of similar vehicle types. Table 5 summarises this comparison, highlighting the proximity of the measured coefficients to published reference ranges and indicating the percentage deviation relative to Hucho's data. Figure 6 shows the experimental distribution of the pressure coefficient (*Cp*) with (w) and without (w/o) the rear wing across a range of Reynolds numbers (Re) along the upper centreline of the car model used in this study. The pressure distribution represents upper-surface measurements only; lower-surface pressures were not recorded, and therefore the integrated drag corresponds to upper-surface contributions only. The pressure decreased over the windscreen and reached another minimum at the transition to the cabin roof, after which it gradually recovered. Specifically, the pressure reached the third low point at the transition between the cabin top and the rear window. Over the rear window and luggage compartment, the pressure recovered. By using the rear wing, there was a difference in pressure distribution close to the rear section of the vehicle for all Reynolds numbers. Increasing the suction, which generates more downforce, a desirable value in CP for improved high-speed stability, was assured. The uncertainty for both cases is somewhat acceptable; the standard uncertainty in Cp is derived from the analytical propagation of the AHJ-501 manometer specification, specifically at a lower Reynolds number of $u(Cp) \approx 0.322$ and at a high Reynolds number of $u(Cp) \approx 0.151$. As a result of using the AHJ-501 manometer, it is ±0.3% FSO, with a 2.999 psi FSO that corresponds to about ±62 Pa absolute errors.

To display the numerical results from this study, Figure 7 represents the numerical flow fields around the 2017 Lamborghini Aventador

Table 5. Comparison of the drag and lift coefficients with Hucho [17]

Vehicle type	CD/CL	Reference Range Hucho[17]	Present (Baseline)	Present modified	Difference (%)
Simplified sports car	CD	0.28–0.36	0.2741	0.2532	Baseline: -2% to -24% Modified: -10% to -30%
Simplified fastback	CL	0.05–0.15	-	0.128	-15% to 156%

LP 750-4 car model, which indicate the main aerodynamic factors that govern drag and lift behaviour. Figure 7(a) shows the velocity vector contour, where the high-speed region above the roof and the weak velocity behind the vehicle can be noticed, resulting in a strong flow separation at the rear. Figure 7(b) shows the streamlines reveal a separation bubble behind the vehicle and flow reattachment along the sides. A low-pressure region forms over the roof and rear window, contributing to the positive lift. Figure 7(c) illustrates the static pressure field. It is clear to signify a low-pressure zone over the roof and rear window, which significantly contributes to the positive lift recorded experimentally and numerically. The upward aerodynamic force forms due to the higher pressure noticed below the body. Figure 7(d) shows the turbulent kinetic energy distribution around the car model. It reveals that elevated turbulence aggregates in the shear layer and in the recirculating weak layer, indicating that separation is the dominant source of unsettledness. The result aligns well with known bluff body aerodynamics and supports the corresponding CL and CD trends obtained from both CFD and experiments.

Finally, the difference between CFD and experimental results for lift coefficient values is below 5%, emphasising the impact of adding a rear wing and illustrating the link between the car's lift coefficient (CL) and Reynolds number (Re). Figure 8 represents the CL with Re. Particularly, at low Re, the car model generates relatively high lift; it decreases steadily with increasing Re for both the experimental and numerical results to 0.8120 and 0.847, respectively. As the Reynolds number increases, the flow becomes more attached and the lift decreases to 0.10–0.13. This indicates better aerodynamic stability at higher speeds.

After installing a rear wing, Hucho reports that the CL for the Volkswagen 1600 with a notchback is 0.18, whereas the best experimental and numerical results of this study were represented at high Re and are 0.128 and 0.105, respectively, due to delayed separation and improved flow reattachment. The aerodynamic surfaces are well-optimised for high-speed circumstances, decreasing lift that could impede traction, as evidenced by the decrease in lift coefficient with rising Reynolds number. Additionally, it emphasises how crucial it is to match aerodynamic elements, such as rear wings, at particular speed ranges to maximise their positive effects on the vehicle's handling and overall performance.

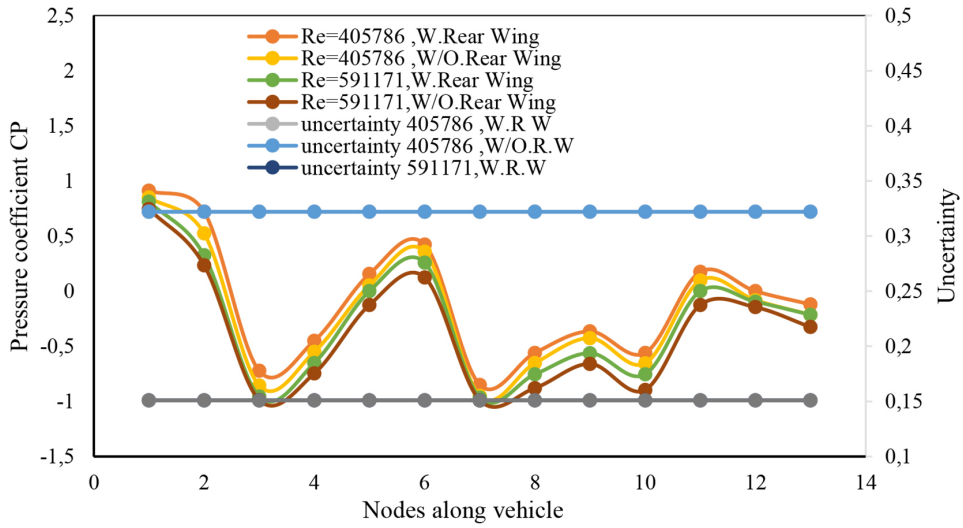

Figure 6. Experimental pressure coefficient (Cp) distribution along the upper centreline of the vehicle, with and without a rear wing, at different Reynolds numbers

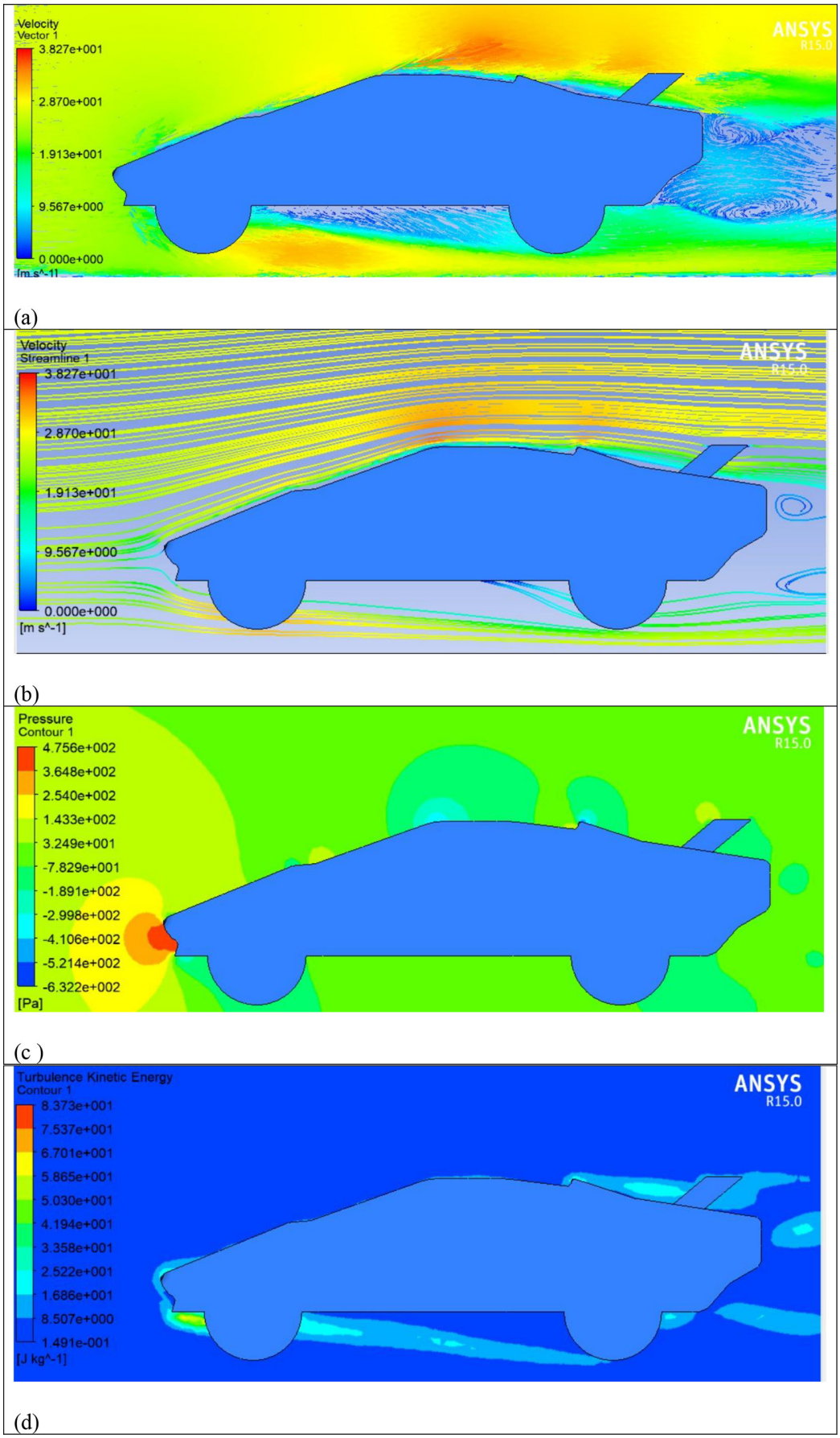

Figure 7. Numerical results (a) velocity vector (b) velocity streamline (c) static pressure (d) turbulent kinetic energy

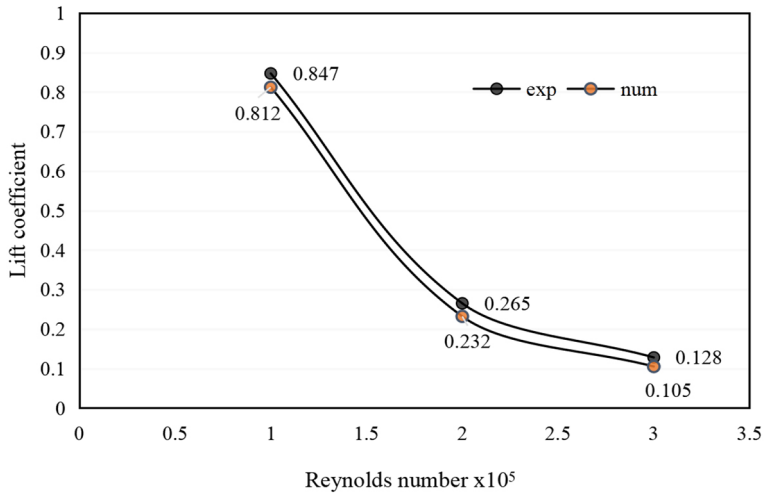

Figure 8. Comparison between experimental and numerical results of the lift coefficient as a function of the Reynolds number

CONCLUSIONS

In this study, the influence of vehicle design geometry on drag reduction was assessed, and the aerodynamic performance of a scaled car model through WT testing was investigated. The results were compared against numerical simulations in two cases, with and without using a rear wing. The findings ascertained the lowest CD across a range of Reynolds numbers. The model performed well in configurations both with and without a rear wing at higher flow regimes, attaining minimum CD values of 0.2836, 0.261, 0.2741, and 0.2532 numerically and experimentally, respectively. In addition, the optimised geometry reduced drag by approximately 3.4% for high Reynolds numbers. The maximum values of the numerical and experimental lift coefficients at high flow regain were 0.105 and 0.128, respectively. For a comparison, Hucho reported a drag coefficient of 0.33 for the Volkswagen 1600 notchback equipped with a rear spoiler, along with notable efficiency gains.

Although only one modification—the rear wing—was introduced, it had a clear effect on wake stabilisation and pressure distribution, especially at higher Reynolds numbers. This in turn would underscore the role of aerodynamic devices in managing downforce and mitigating flow separation. Furthermore, the average difference between CFD and the experimental lift coefficient is about 4% at lower Reynolds numbers. The experimental outcomes offer valuable insights for full-scale vehicle design and align with established aerodynamic theory. The numerical simulations for lift and drag coefficients showed a good agreement with experimental measurements over a wide range of Reynolds numbers, therefore, the results do have some limitations since the model geometry is fairly basic, and there are some uncertainties with the experimental measurements. Despite these issues, the analysis still provides some cool insights into aerodynamic trends and how tweaks to the rear wing impact them.

Acknowledgements

The authors express deep gratitude to the mechanical engineering department of the University of Diyala for their continuous support and assistance in using the wind tunnel (WT) facility, especially Engineers Hind J. and Mustafa for their help with this work.

REFERENCES

1. Al-Saadi A., Al Farhany K., Kadhim K., Al Chlaihawi I., Jamshed W., Mohamed R., El Sayed M., and Raizah Z. Improvement of the aerodynamic behaviour of a sport utility vehicle numerically by using some modifications and aerodynamic devices, Sci. Rep., 2022; 12(1): 1–14. https://doi.org/ 10.1038/s41598-022-24328-w
2. Junaidin B. Aerodynamic analysis of sport utility vehicle (SUV) by computational fluid dynamics (CFD) approach, Vortex, 2022; 3(1): 67. https://doi.org/10.28989/vortex.v3i1.1161
3. Bonnavion G., Borée J., and Herbert V. On the use of kinetic energy balance for the volumetric identification of drag sources of a blunt body: Application to road vehicles, Int. J. Heat Fluid Flow, 2022; 96: 1–16. https://

doi.org/10.1016/j.ijheatfluidflow.2022.108977

4. Huluka A. and Kim C. Numerical study on aerodynamic drag reduction and energy harvest for electric vehicle: A concept to extend driving range, IOP Conf. Ser. Mater. Sci. Eng., 2019; 700(1). https://doi.org/10.1016/j.rineng.2025.105489
5. Bauskar M. P., Dhande D. Y., Vadgeri S., and Patil S. R. Study of aerodynamic drag of sports utility vehicle by experimental and numerical method, Mater. Today, Proc., 2019; 16: 750–757. https://doi.org/10.1016/j.matpr.2019.05.155
6. Wieser D., Schmidt H. J., Müller S., Strangfeld C., Nayeri C., and Paschereit C. Experimental comparison of the aerodynamic behaviour of Fastback and Notchback DrivAer models, SAE Int. J. Passeng. Cars - Mech. Syst., 2014; 7(2): 682–691. https://doi.org/10.4271/2014-01-0613
7. Qin P., Ricci A., Blocken B. CFD simulation of aerodynamic forces on the DrivAer car model: Impact of computational parameters, Journal of Wind Engineering and Industrial Aerodynamics, 2024; 248. https://doi.org/10.1016/j.jweia.2024.105711
8. Gan Y., Li L. Optimisation of aerodynamic profile of ground vehicle, Journal of Physics: Conference Series 2023; 2569(1). https://doi.org/ 10.1088/1742-6596/2569/1/012068
9. Desai M., Channiwala S., Nagarsheth H. Experimental and Computational Aerodynamic Investigations of a Car, 6th Iasme/Wseas International Conference on Fluid Mechanics and Aerodynamics (Fma'08) Rhodes, Greece, August 20–22, 2008**.**
10. Ramasamy D., Mohanesan K., Kadirgama K., Noor M. M., and Rahman M. M. Hybrid electric vehicle car body drag analysis using computational fluid dynamics, Int. J. Automot. Mech. Eng., 2017; 14(3): 4496–4507. https://doi.org/10.15282/ijame.14.3.2017.8.0355
11. Baek S., Lee S. Aerodynamic drag reduction on a realistic vehicle using continuous blowing, Microsystem Technologies 2020; 26(1): 11–23. https://doi.org/10.1007/s00542-019-04355-w
12. Varun R., Sankar S., Varma R., Sreejith K.V. CFD Analysis of aerodynamics of car, International Journal of Innovative Research in Science 2018; 7(5). https://doi.org/10.15680/IJIRSET.2018.0705037
13. Delassaux F., Herbert V., Mortazavi I. and Ribes C. Numerical investigation of the flow around simplified ground vehicles using hybrid RANS/LES method, Notes Numer. Fluid Mech. Multidiscip. Des., 2020; 143: 357–365. https://doi.org/10.1007/978-3-030-27607-2_29
14. Almahdawi Y. A., Abbas Mohammed K. H., Al-Samari A., Aldabash N., Hafedh S. A. Temperature effect in the energy degradation of photovoltaic power temperature effect in the energy degradation of photovoltaic power Journal of Thermal Engineering, 2023; 9(5): 1153–1162. https://doi.org/10.18186/thermal.1370726
15. Mohammadi M., Nazemosada S., Faze D. and Lari Y. An integrated approach for structural modeling, modal analysis, and aerodynamic evaluation of an electric vehicle body shell using finite element method and computational fluid dynamics. Materials Today Communications, 2025; 45: 112331. https://doi.org/10.1016/j.mtcomm.2025.112331
16. Nowakowski M., Kosiuczenko K. Evaluation of TAERO UGV structural collision resistance using FEM analysis, Bulletin of the Polish Academy of Sciences, Mechanical and Aeronautical Engineering, Thermodynamics, Technical Sciences, 2025; 73(3): E153431. https://doi.org/10.24425/bpasts.2025.153431
17. Hucho W. H. Aerodynamics of Road Vehicles, Cambridge University Press. 1986.
18. Altinisik A., Kutukceken E. and Umur H. Experimental and numerical aerodynamic analysis of a passenger car: Influence of the blockage ratio on drag coefficient, J. Fluids Eng. Trans. ASME, 2015; 137(8). https://doi.org/10.1115/1.4030183
19. Hatem F., Abbas Mohammed K. H. Alhumairi, Al-Obaidi M., Mohammad A. and Darwish A. Upgrading gas turbine efficiency for sustainable power generation: An energy and exergy analyses, Results Eng., 2025; 26: 2024–2026. https://doi.org/10.1016/j.rineng.2025.105489
20. Wang, Xin Y. Y., Gu Zh., Wang Sh., Deng Y. and Yang X. Numerical and experimental investigations on the aerodynamic characteristic of three typical passenger vehicles, Journal of Applied Fluid Mechanics. 2014. https:// doi.org/10.36884/jafm.7.04.21460
21. Maskell E. A theory of the blockage effects on bluff bodies and stalled wings in a closed wind tunnel ARC, R + M 3400, 1961, London.
22. Mercker E. A blockage correction for automotive testing in a wind tunnel with closed test section. Journal of Wind Engineering and Industrial Aerodynamics, 1986; 22(149–167): 149.
23. Fu C., Uddin M., and Zhang C. Computational analyses of the effects of wind tunnel ground simulation and blockage ratio on the aerodynamic prediction of flow over a passenger vehicle. Vehicles 2020; 2: 318–341. https://doi.org/10.3390/vehicles2020018